



## RESEARCH COMMUNICATION

# Temporal correlation of morphological and biochemical changes with the recruitment of different mechanisms of reactive oxygen species formation during human SW872 cell adipogenic differentiation

Mara Fiorani  | Rita De Matteis | Barbara Canonico | Giulia Blandino |  
Alessandro Mazzoli | Mariele Montanari | Andrea Guidarelli | Orazio Cantoni 

Department of Biomolecular Sciences,  
University of Urbino Carlo Bo, Urbino,  
Italy

## Correspondence

Mara Fiorani, Dipartimento di Scienze  
Biomolecolari, Sezione di Biochimica e  
Biotecnologie, Università degli Studi di  
Urbino, Via Saffi 2, 61029 Urbino (PU),  
Italy.

Email: mara.fiorani@uniurb.it

## Funding information

Ministero della Salute, Grant/Award  
Number: RF-2016-02363761

## Abstract

Human SW872 preadipocyte conversion to mature adipocytes is associated with time-dependent changes in differentiation markers' expression and with morphological changes accompanied by the accumulation of lipid droplets (LDs) as well as by increased mitochondriogenesis and mitochondrial membrane potential. Under identical conditions, the formation of reactive oxygen species (ROS) revealed with a general probe was significant at days 3 and 10 of differentiation and barely detectable at day 6. NADPH oxidase (NOX)-2 activity determined with an immunocytochemical approach followed a very similar pattern. There was no evidence of mitochondrial ROS (mROS), as detected with a selective fluorescence probe, at days 3 and 6, possibly due to the triggering of the Nrf-2 antioxidant response. mROS were instead clearly detected at day 10, concomitantly with the accumulation of very large LDs, oxidation of both cardiolipin and thioredoxin 2, and decreased mitochondrial glutathione. In conclusion, the morphological and biochemical changes of differentiating SW872 cells are accompanied by the discontinuous formation of ROS derived from NOX-2, increasingly implicated in adipogenesis and adipose tissue dysfunction. In addition, mROS formation was significant only in the late phase of differentiation and was associated with mitochondrial dysfunction.

## KEYWORDS

adipocyte differentiation, mitochondria, NADPH oxidase, ROS

**Abbreviations:** 3-IBMX, 3-isobutyl-1-methylxanthine; C/EBPs, CAAT/enhancer-binding proteins; DCF, chloromethyl-2',7'-dichlorodihydrofluorescein diacetate; DM, differentiation medium; DTNB, dithiobis-2-nitrobenzoic acid; FSC, forward scatter; LD, lipid droplet; mGSH, mitochondrial glutathione; mROS, mitochondrial ROS; MTG, MitoTracker Green; NAO, nonyl acridine orange; NOX, NADPH oxidase; NR, Nile Red; Nrf2, nuclear factor (erythroid-derived 2)-like 2; ORO, Oil Red O; PPAR $\gamma$ , peroxisome proliferator-activated receptor  $\gamma$ ; PVDF, polyvinylidenedifluoride; ROS, reactive oxygen species; SDS, sodium dodecyl sulfate; SSC, side scatter; TMRE, tetramethylrhodamine; Trx2, thioredoxin 2.

This is an open access article under the terms of the Creative Commons Attribution-NonCommercial-NoDerivs License, which permits use and distribution in any medium, provided the original work is properly cited, the use is non-commercial and no modifications or adaptations are made.

© 2021 The Authors. *BioFactors* published by Wiley Periodicals LLC on behalf of International Union of Biochemistry and Molecular Biology.

## 1 | INTRODUCTION

Adipose tissue plays an essential role in maintaining lipid and glucose homeostasis. More specifically, healthy adipose tissue is actively engaged in the regulation of nutrient excess removal from the bloodstream as well as in storing/releasing of energy. This is in remarkable contrast with adipose tissue dysfunction that links obesity to related metabolic diseases.<sup>1–3</sup> These conditions, in which oxidative stress is increasingly implicated,<sup>4,5</sup> are particularly relevant for the human health, since associated with an increased risk for many chronic disorders, as hypertension, type II diabetes, cardiovascular diseases, and some types of cancer.<sup>6,7</sup>

A deeper understanding of the mechanisms involved in the process of adipogenesis and regulation of adipocyte function/malfunction is therefore critical for the comprehension of the molecular basis of these metabolic diseases. Based on the current knowledge, adipogenesis can be defined as a highly regulated-multistep process, mediating proliferation and differentiation of mesenchymal stem cells to lipid-laden mature adipocytes. It involves expression of genes and transcriptional factors, as the CAAT/enhancer-binding proteins (C/EBPs) family, peroxisome proliferator-activated receptor  $\gamma$  (PPAR $\gamma$ ), cell cycle regulatory proteins, hormones, and growth factors.<sup>8,9</sup>

The formation of reactive oxygen species (ROS) is critical for adipocyte differentiation and, consistently, this process was inhibited or suppressed by antioxidants, as *N*-acetyl-L-cysteine or vitamin C.<sup>10,11</sup> The specific role of these species, however, is still controversial and in general poorly understood.<sup>12,13</sup> Excess of nutrients has been associated with an extensive mitochondrial ROS (mROS) formation<sup>14,15</sup> as well as with activation of NADPH oxidases (NOX) during adipogenesis.<sup>15,16</sup>

NOX-4, the most abundant NOX in mature adipocytes,<sup>15,16</sup> is constitutively active and independent of activator proteins,<sup>13</sup> redox regulated by its own product,<sup>17</sup> directly generates H<sub>2</sub>O<sub>2</sub> under basal conditions and hence responsible for long-lasting effects.<sup>18,19</sup> Furthermore, preadipocytes and mature adipocytes express other NOX enzymes,<sup>15,16</sup> which include the phagocytic NOX-2, comprising six different subunits in part integrated in the plasma membrane and in part localized in the cytosol.<sup>16</sup> After appropriate stimuli, these subunits interact to release superoxide (O<sub>2</sub><sup>•-</sup>) in both intracellular and extracellular compartments. NOX-2 is also expressed in nonphagocytic cells, including human primary as well as rodent adipocytes.<sup>20,21</sup> Interestingly, NOX-2 deletion mitigates adiposopathy induced by a high fat diet in experimental animals,<sup>22,23</sup> in contrast to NOX-4 deficiency, which produced opposite effects.<sup>24</sup>

The process of adipogenesis has been extensively studied in primary cells in culture, an approach presenting the advantage of the biological relevance of the experimental results, and also some disadvantages in particular associated with the limited availability and renewal capacity of the cells.<sup>25</sup> In order to overcome these drawbacks, there has been a continuous increase in the use of cultured cells, in particular the murine 3T3-L1 cell line.<sup>26</sup> This well-characterized cellular model of adipogenesis, while conveniently utilized by numerous authors,<sup>26–29</sup> however, presents some limitations related to the translation of the experimental outcomes to humans.<sup>12,30–33</sup> Based on these considerations, it appears important to establish and characterize paradigms of adipogenesis using human cultured cells.

In recent years, there has been a growing interest in the use of SW872 cells, derived from a human liposarcoma,<sup>31,34–38</sup> which however remain poorly characterized for several aspects, in particular related to the identification of the specific mechanisms associated with ROS formation during adipogenesis.

Using this cell line, we performed a detailed characterization of the morphological and biochemical changes occurring during adipocyte differentiation and identified early events leading to NOX-2 activation followed by late mROS formation and dysfunction.

## 2 | MATERIALS AND METHODS

### 2.1 | Materials

Acrylamide 30%, glycine, sodium dodecyl sulfate (SDS), methanol, acetonitrile, insulin, dexamethasone, 3-isobutyl-1-methylxanthine (3-IBMX), oleic acid-albumin and linoleic acid-albumin, Oil Red O (ORO), glutathione (GSH), dithiobis-2-nitrobenzoic acid (DTNB), isopropanol, and most of the reagent-grade chemicals were purchased from Merck Life Science s.r.l. (Milan, Italy). Sodium chloride, ethylenediaminetetraacetic acid (EDTA), Na<sub>2</sub>HPO<sub>4</sub>, KH<sub>2</sub>PO<sub>4</sub>, and K<sub>2</sub>HPO<sub>4</sub> were from Carlo Erba (Milan, Italy). Tween 20 and WesternBright ECL (K12045) were purchased from Advansta-Aurogenes s.r.l. (Rome, Italy). Clarity Max was purchased from BioRad Laboratories s.r.l. (Milan, Italy).

### 2.2 | Cell culture conditions

Human liposarcoma SW872 cells were purchased from the American Type Culture Collection (Rockville, MD) and used between passages 3 and 10. Cells were maintained in Dulbecco's modified Eagle medium/

nutrient mixture F-12 (DMEM/F12) Merck Life Science s.r.l. (Milan, Italy), supplemented with 10% fetal bovine serum (FBS) (35-079-CV, Corning-S.I.A.L. s.r.l, Rome, Italy), 100 U/ml penicillin, 100 µg/ml streptomycin (P4333, Merck Life Science s.r.l. Milan, Italy), under a humidified 5% (vol/vol) CO<sub>2</sub> atmosphere at 37°C.

Postconfluent SW872 cells were induced to differentiation by changing the medium with the differentiation medium (DM) composed of 1 µM dexamethasone, 0.1 mM 3-IBMX, 30 µM bovine serum albumin (BSA)-bounded oleic acid/linoleic acid, and 10 µg/ml insulin in DMEM/F12 with 10% FBS). The DM was changed every 48 h and the differentiation process was followed up to day 10.<sup>33</sup> Morphological, immunocytochemical, and biochemical analyses were performed at different time points of SW872 cell differentiation.

### 2.3 | Cell culture preparation for morphological analysis

The SW872 cells were seeded onto 12-mm sterile glass microslides (Thermo Fisher Scientific, United Kingdom) placed inside the 12-well plates and differentiated, as described in the previous paragraph.

### 2.4 | ORO staining

In cellular preparations, neutral lipids were visualized using the soluble selective dye ORO.<sup>39</sup> Slides were washed with potassium phosphate-buffered saline (PBS: 136 mM NaCl, 10 mM Na<sub>2</sub>HPO<sub>4</sub>, 1.5 mM KH<sub>2</sub>PO<sub>4</sub>, 3 mM KCl; pH 7.4) and fixed for 1 h with 4% paraformaldehyde in PBS at 4°C, washed in the same buffer, and then incubated in 0.3% ORO solution, as previously described.<sup>39</sup>

The slides were incubated with the ORO working solution for 1 h at room temperature, washed twice with H<sub>2</sub>O, counterstained with hematoxylin to visualize nuclei, and mounted in glycerol gel (Sigma-Aldrich-SIAL Rome, Italy).

### 2.5 | Western blot assay

Equal amounts (40 µg) of cell lysates were resolved in 8–12% SDS polyacrylamide gel and electrotransferred to polyvinylidene difluoride (PVDF) membranes. Western blot analyses were performed using antibodies against actin, C/EBPβ, C/EBPδ, PPARγ, CD36, and nuclear factor (erythroid-derived 2)-like 2 (Nrf2) (Table S1). Details on the Western blotting apparatus and conditions are reported elsewhere.<sup>40</sup>

### 2.6 | Redox Western blot analysis

The thioredoxin2 (Trx2) redox state was estimated by redox Western blots, as described by Guidarelli et al.<sup>41</sup> Briefly, at the indicated time points, the cells were washed with PBS and detached from the culture dish in 200 µl urea lysis buffer (100 mM Tris/HCl, pH 8.2; urea 8 M; EDTA 1 mM) containing 10 mM iodoacetamide. The samples were then incubated for 20 min at 37°C and centrifuged for 1 min at 14,000g. Ten volumes of cold acetone/1 M HCl (98:2) were added to the supernatants and the pellets were washed twice with acetone/1 M HCl/H<sub>2</sub>O (98.2:10). The pellets were resuspended in 80 µl of urea lysis buffer containing 3.5 mM dithiothreitol, and, after a 30 min incubation at 37°C, incubated for a further 30 min at the same temperature in the presence of 30 mM iodoacetamide. Samples were then subjected to urea polyacrylamide gel electrophoresis (7 M urea and 7% acrylamide), under nonreducing conditions, and blotted.<sup>42</sup>

### 2.7 | Isolation of mitochondria

Cells were processed to obtain a crude mitochondrial fraction, as described by Fiorani et al.<sup>43</sup> Briefly, the cells were washed twice in PBS and detached with pre-warmed trypsin/EDTA solution (2.5 g/L trypsin plus 0.2 g/L EDTA). The cells were then transferred to a centrifuge tube, washed with PBS, and resuspended in ice-cold homogenization buffer (HB, 225 mM mannitol, 75 mM sucrose, 0.1 mM EGTA, protease inhibitor cocktail, 5 mM Tris-HCl, pH 7.4). The cells were homogenized with 30–40 strokes in a glass potter placed in an ice-bath. The efficiency of the homogenization process was monitored under the microscope by counting the number of residual trypan blue negative cells. The homogenate was centrifuged at 1000g for 10 min at 4°C and the supernatant (S1) was collected for the final centrifugation. The pellet was rehomogenized and the supernatant (S2) was added to S1 and centrifuged at 12,000g for 30 min at 4°C. The corresponding pellet (mitochondrial fraction) was washed and processed for GSH analysis.

### 2.8 | Measurement of GSH content in cells and mitochondria by high-performance liquid chromatography

GSH content in SW872 cells and mitochondria was measured as described by Fiorani et al.<sup>40</sup> Briefly, the cellular or mitochondrial pellets were suspended in lysis buffer (0.1% Triton X-100; 0.1 M Na<sub>2</sub>HPO<sub>4</sub>; 5 mM Na-EDTA, pH 7.5), vortexed, and kept for 10 min on an ice bath.

Thereafter, 0.1 N HCl and precipitating solution (0.2 M glacial meta-phosphoric acid, 5 mM Na-EDTA, 0.5 M NaCl) were added to the samples. After centrifugation, the supernatants were collected and kept at  $-20^{\circ}\text{C}$  until the high-performance liquid chromatography (HPLC) analyses. Just before analysis, DTNB (20 mg in 100 ml of 1% wt/vol sodium citrate) was added to the extracts. The samples were filtered through 0.22- $\mu\text{m}$ -pore microfilter and finally analyzed for their GSH content by HPLC,<sup>44</sup> using a 15 cm  $\times$  4.6 mm, 5  $\mu\text{m}$  Supelco Discovery<sup>®</sup> C18 column (Supelco, Bellefonte, PA). The UV absorption was detected at 330 nm. The injection volume was 20  $\mu\text{l}$ . The retention time of GSH was  $\sim$ 15.7 min.

## 2.9 | Flow cytometric staining

Cells were labeled with one of the indicated fluorochromes. MitoSOX Red (5  $\mu\text{M}$ , 10 min), a dye targeting the mitochondria of live cells, is selectively oxidized by  $\text{O}_2^-$  to produce red fluorescence,<sup>45</sup> chloromethyl-2',7'-dichlorodihydrofluorescein diacetate (DCF, 5  $\mu\text{M}$ , 30 min), a general probe for ROS detection.<sup>46</sup> The mitochondrial membrane potential was analyzed using tetramethylrhodamine (TMRE, 40 nM, 15 min), selectively taken up by mitochondria.<sup>47</sup> MitoTracker Green (MTG, 50 nM, 30 min) is taken up by mitochondria independently of their membrane potential.<sup>47</sup> The cardiolipin-sensitive probe 10-nonyl acridine orange (NAO, 100 nM, 15 min) was used to monitor mitochondrial lipid changes.<sup>47</sup> Nile Red (NR, 1  $\mu\text{g}/\text{ml}$  in dimethylsulfoxide, 15 min) is a phenoxazine dye, which can be used to localize and quantify neutral and polar lipids in living cells. Polar lipids (i.e., phospholipids), mostly present in membranes, are stained in red (emission  $>590$  nm), whereas neutral lipids (esterified cholesterol and triglycerides), present in lipid droplets (LDs), are stained in yellow (570–590 nm).<sup>47</sup> At least 10,000 events were acquired for each sample.

## 2.10 | DNA content analysis

The effects on cell cycle progression were investigated in differentiating SW872 cells by flow cytometry, as previously detailed by Benedetti et al.<sup>48</sup>

## 2.11 | Cytometric investigations

Cytometric experiments were carried out with a FACS Canto II flow cytometer equipped with an argon laser (blue, Ex 488 nm), a helium-neon laser (red, Ex 633 nm)

and a solid-state diode laser (Violet, Ex 405 nm). Analyses were performed by using FACSDiva<sup>™</sup> software;  $\sim$ 15,000 cell events were acquired for each sample.

## 2.12 | Immunofluorescence analysis

The cells were fixed for 1 min with 95% ethanol/5% acetic acid, washed with PBS, and blocked in PBS-containing BSA (2% wt/vol) (30 min at room temperature). The cells were subsequently incubated with rabbit polyclonal antiphosphorylated p47<sup>phox</sup> (Table S1), stored for 18 h at  $4^{\circ}\text{C}$ , washed, and then incubated for 3 h in the dark with fluorescein isothiocyanate (Santa Cruz Biotechnology)-conjugated secondary antibody diluted 1:100 in PBS. The cells were washed three times and fluorescence images were captured using a BX-51 microscope (Olympus, Milan, Italy), equipped with a SPOT-RT camera unit (Diagnostic Instruments, Delta Sistemi, Rome, Italy) using an Olympus LCAch 40  $\times$  0.55 objective lens. The excitation and emission wavelengths were 488 and 515 nm with a 5-nm slit width for both emission and excitation.

## 2.13 | Immunocytochemistry

Cells grown on microslides were fixed in 4% formaldehyde in PBS (15 min), washed twice in PBS and permeabilized (10 min) in PBS containing 0.25% Triton-X 100, or washed in PBS when permeabilization was not required. After fixation and permeabilization, cells were blocked with 2% normal serum at room temperature for 20 min. Immunostaining was carried out with specific primary antibodies (Table S1). The immunoreaction was revealed with the avidin–biotin–peroxidase complex (ABC) method (Vector, Burlingame, CA, United States). Peroxidase activity was revealed by diaminobenzidine hydrochloride as chromogen (Sigma-Aldrich—SIAL, Rome, Italy). The cellular preparations were then counterstained with methyl green (Genetex-Prodotti Gianni, Milan, Italy) and mounted in Eukitt (Kindler, Freiburg, Germany).

Preparations were examined using a Nikon light microscope (Nikon Eclipse 80i microscope, Laboratory Imaging, Czech Republic) and an ACT-2U image analyzer linked to a Sony equipped with digital camera.

## 2.14 | Statistical analysis

Data are expressed as mean  $\pm$  SD. Comparisons were made using a one-way analysis of variance (ANOVA)



followed by Dunnett's test for multiple comparison. All experiments were repeated at least three times. Differences were considered significant at  $p < 0.05$  (\*) and  $p < 0.01$  (\*\*).

### 3 | RESULTS

#### 3.1 | Morphological changes of differentiating SW872 cells

Addition of the DM to confluent SW872 cells promoted adipogenesis associated with significant time-dependent changes in morphology. Cells, initially displaying a fibroblast-like morphology, virtually in the absence of detectable lipid accumulation (Figure 1A, T0), became more elongated at day 3 (T3), with some LDs in their cytoplasm. At day 6 of differentiation (T6), the cells featured a more rounded shape, with an increased number and size of LDs dispersed throughout the cytosol. At day 10 (T10), most cells appeared roundish with large LDs, thereby displaying the typical morphology of mature adipocytes.

The time-dependent conversion of preadipocytes to fully differentiated adipocytes can be well appreciated by the analysis of the results illustrated in Figure 1B, in which the LD total area per cell was quantified with the “analyse particles” function of the ImageJ software.<sup>49</sup> Spectrophotometric measurement of ORO eluted from the cells also provided an indication for a time-dependent increase of intracellular lipid content during differentiation, however with a slowdown of the lipid accumulation trend after the sixth day (Figure 1B).

It is important to note that the above changes were detected in the very last majority of the cells analyzed at the different time points of differentiation. However, a small proportion of cells at different stages of differentiation was detected in all of these conditions. An example is provided by cultures at T10, characterized by a large proportion of rounded cells with an abundant lipid accumulation, and also by other cells more elongated and with a significantly lower LD content (Figure 1A). This notion was more clearly established by comparing flow cytometric forward scatter (FSC) versus side scatter (SSC) dot plots in cells at T0 versus T10 (Figure 1C), using a procedure employed in other studies.<sup>50</sup> Quantification of these data (Figure 1D) demonstrates that at T6 most of the cells correspond to mature adipocytes, falling in the SSC zone (P2, about 80%), whereas the less differentiated phenotype accounted for the residual 20% of the cell population (P1). Remarkably similar results were obtained at day 10, thereby suggesting that differentiation was nearly completed at day 6 (Figure 1C,D).

Figure 1E depicts a representative histogram plot for NR staining in P2 cell population (i.e., blue area enclosed cells). Histogram overlay shows an increase in NR fluorescence intensities from blue events enclosed in the P2 area, highlighting the presence of scarce and dim-fluorescent cells at T0 (red histogram on the left). The lipid quantification of both P1- and P2-enclosed cells reported in Figure 1F reveals a similar lipid accumulation trend in both subpopulations, but a significantly higher amount of LDs in P2 cells. These results indicate that a flow of cells from P1 red to the P2 blue area occurred during differentiation (Figure 1C), and that the increase in the granulation/vacuolation of these cells is paralleled by an increased lipid content (Figure 1E).

#### 3.2 | Cell cycle distribution and expression of adipogenic markers during SW872 cell differentiation

We measured the changes in DNA content and cell cycle distribution of differentiating SW872 cells. As indicated by the analysis of the flow cytometric DNA profiles reported in Figure 2A, there was evidence for a time-dependent reduction in the number of proliferating cells, which appeared well synchronized at T10, with a large prevalence of cells in the G0/G1 phase (>90%).

The expression patterns of specific transcription factors and differentiation markers were next analyzed by both Western immunoblotting (Figure 2B) and immunocytochemistry (Figure 2C).

We found that C/EBP $\beta$ , a “classical” early inducer of adipogenesis,<sup>8,9</sup> is constitutively expressed and largely localized in the nuclei of cells at T0, upregulated at T3 and T6, with a return to control levels at T10. Increased expression of C/EBP $\beta$  protein was in most cells associated with both nuclear and diffused cytoplasmic labeling.

C/EBP- $\delta$  was instead barely detectable at T0 and T3, but its expression eventually increased significantly (four times) at T6 and T10. Immunocytochemical analysis revealed that T0 cells exclusively express nuclear C/EBP $\delta$ , with a progressive decline at T3–T10, in parallel with a redistribution of the protein in the cytoplasm. Rounded T6 or T10 cells, in particular when associated with an elevated lipid accumulation, showed a weak cytoplasmic C/EBP $\delta$  staining.

PPAR $\gamma$  expression, very low at T0, was significantly increased at T3, to remain to similar levels throughout the entire course of the differentiation period. PPAR $\gamma$  was mainly localized in the nuclear compartment. CD36, a target gene of PPAR $\gamma$ ,<sup>8,9</sup> followed the same expression pattern of PPAR $\gamma$ , but with a different subcellular distribution. CD36 immunoreactivity was indeed generally diffused and occasionally punctate or even reticular.

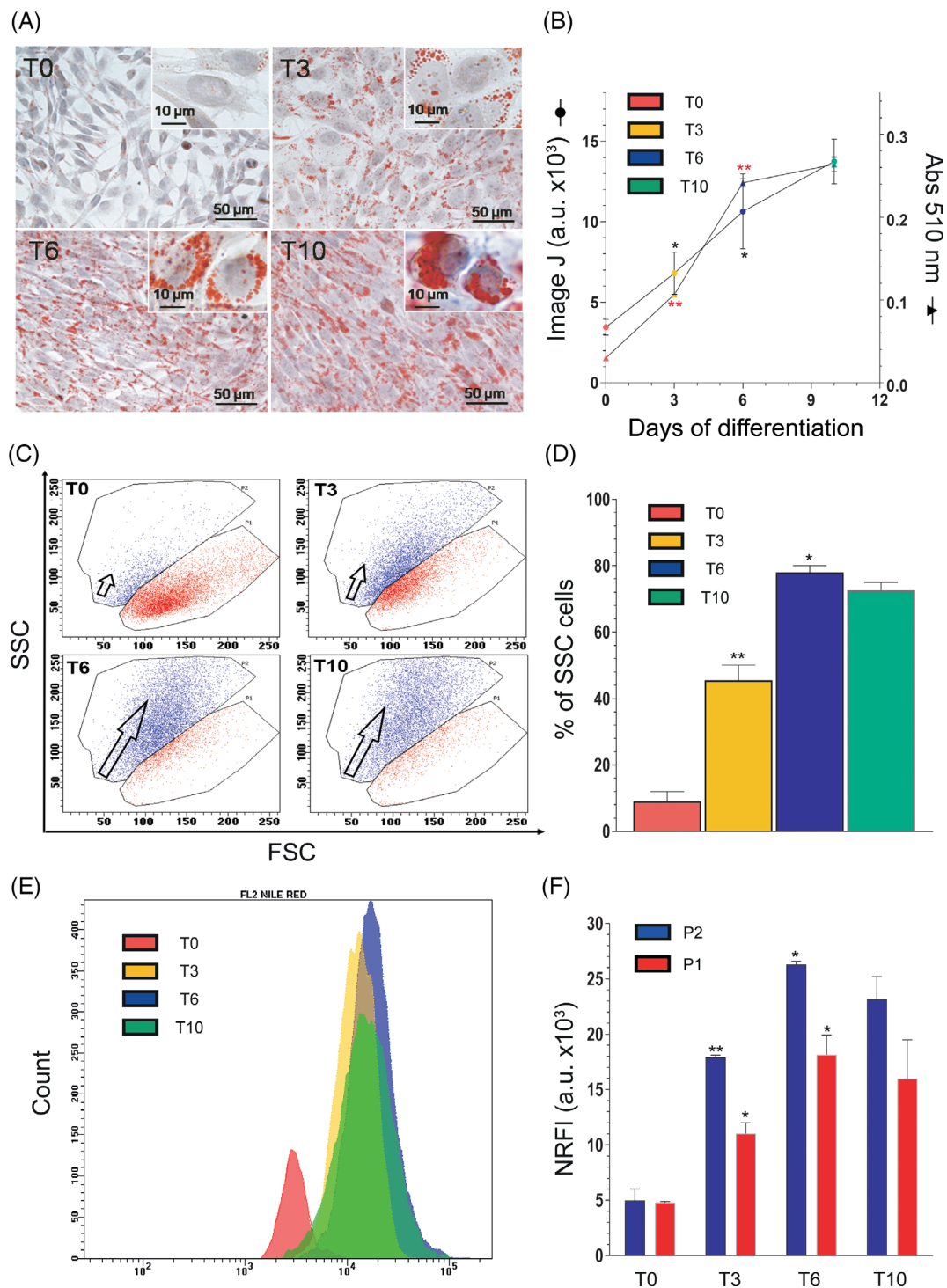


**FIGURE 1** Morphological changes in differentiating SW872 cells. (A) Representative images of Oil Red O (ORO)-stained LDs (red) and hematoxylin-stained nuclei (blue), in differentiating SW872 cells. The higher enlargements (insets) allowed to analyze the differences of lipid accumulation in the cytoplasm of the cells: (T0) tiny LD accumulation; (T3) a substantial lipid accumulation as small LDs; (T6) numerous enlarged LDs; (T10) some large lipid vacuoles in fully differentiated adipocytes. Bars = 50  $\mu\text{m}$ ; inset = 10  $\mu\text{m}$ . (B) Cellular ORO quantification performed by ImageJ software and by spectrophotometric analysis. (C) Forward scatter (FSC) versus side scatter (SSC) dot plots at the indicated differentiation times. The red area enclosed by gate P1 at T0 represents highly enriched events. Of note, the blue area (enclosed by gate P2) progressively becomes the main representative of total cells, particularly at T6 and T10. The blue area is characterized by an increase in SSC values, meaning an increase in granulations/vacuolations in each cell, as explained in the text. (D) Statistical analysis of the percentage of SSC cells (granulated/vacuolated cells) at the indicated differentiation times. (E) Representative histogram of Nile Red-labeled cells from P2 blue area. (F) Comparison between fluorescence intensities (NR FI) from blue events, enclosed in the P2 gate (more differentiated cells) and red events, enclosed in the P1 gate (less differentiated cells). Values reported are raw FI data of specific FL2 Nile Red fluorescence (revealing neutral lipid). Results represent the means  $\pm$  SD calculated from at least three independent determinations. \* $p < 0.05$ , \*\* $p < 0.01$ , as compared to the previous time point (one-way analysis of variance followed by Dunnett's test)

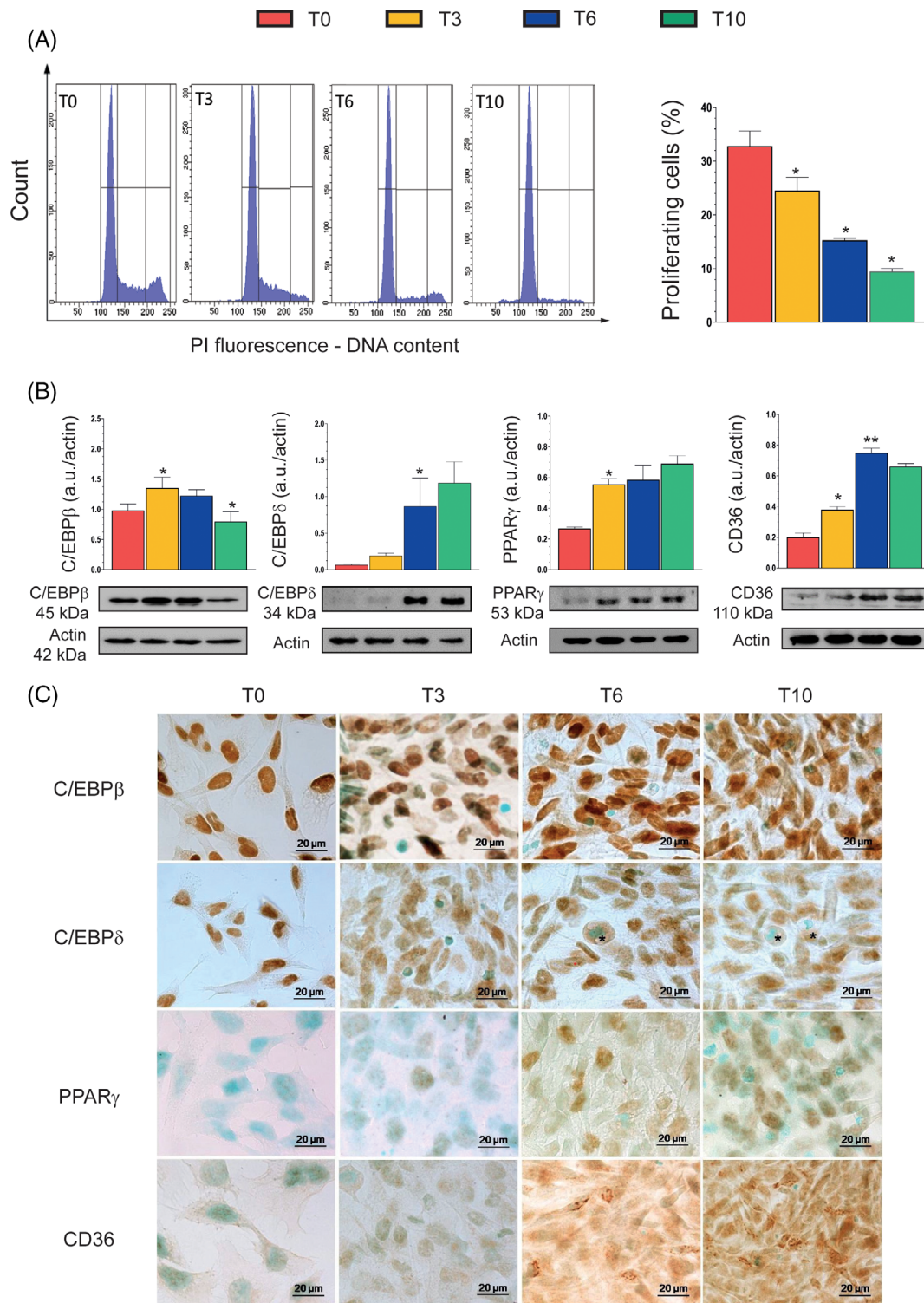


**FIGURE 2** Proliferation state and expression of adipogenic markers during differentiation. (A) DNA content of cells at different stages of differentiation was evaluated by flow cytometry. Histogram profiles highlight the progressive loss of proliferating cells during the process of differentiation. Markers are posed in sequence to delineate (and quantitate) G0/G1, S, and G2/M phases. Events from S+G2/M phases (proliferating cells) were calculated and plotted in the statistic histogram. (B) Western immunoblotting analysis of the key adipocyte differentiation markers CAAT/enhancer-binding protein β (C/EBPβ), C/EBPδ, peroxisome proliferator-activated receptor γ (PPARγ), and CD36, at the indicated differentiation times. Actin was used as a loading control. (C) Immunohistochemical analysis of C/EBPβ, C/EBPδ, PPARγ, and CD36 at the indicated differentiation times. Immunolocalization was visualized using diaminobenzidine (brown) and nuclei were counterstained with methyl green. \* indicates adipocyte with evident lipid accumulation. Magnification 100×; bar: 20 μm. Results represent the means ± SD calculated from at least three independent determinations. \**p* < 0.05, \*\**p* < 0.01, as compared to the previous time point (one-way analysis of variance followed by Dunnett's test)



### 3.3 | Increase in mitochondrial mass/number and membrane potential during SW872 cell differentiation

We simultaneously measured MTG and TMRE fluorescence in differentiating SW872 cells to obtain an indication of the relative mitochondrial mass/number and mitochondrial membrane potential, respectively. As indicated in Figure 3A, MTG exhibits fluorescence progressively, but moderately increased with time of differentiation. The TMRE fluorescence response was

instead steeper and indicative of a significant rise in mitochondrial membrane potential.

In other experiments, the use of a different fluorescent probe, NAO, revealed a progressive increase in cardiolipin content from day 0 to day 6 (Figure 3B), consistently with the observed increase in mitochondrial mass/number (Figure 3A). However, a sudden drop of NAO fluorescence occurred at T10, which obviously does not fit with the data demonstrating a further increase in mitochondrial mass/number, and might rather provide an indication of cardiolipin oxidation.<sup>51</sup>

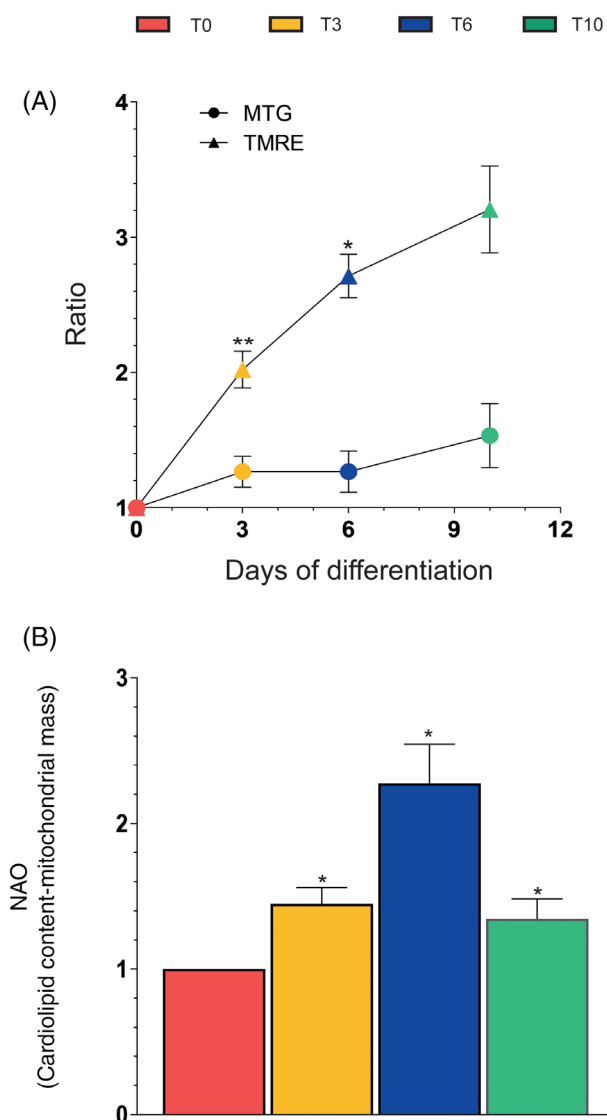


**FIGURE 3** Flow cytometric analyses of mitochondrial mass and membrane potential during differentiation. (A) MitoTracker Green (MTG)- and tetramethylrhodamine (TMRE)-fluorescence intensity (FI) assays and (B) NAO-FI analysis at the indicated differentiation times. Results are the ratio T3-T10/T0 and represent the means  $\pm$  SD calculated from at least three independent determinations. \* $p$  < 0.05, \*\* $p$  < 0.01, as compared to the previous time point (one-way analysis of variance followed by Dunnett's test)

### 3.4 | ROS formation during SW872 cell differentiation

We measured ROS formation in differentiating SW872 cells using DCF. Figure 4A shows representative cytometric profiles for the DCF fluorescence detected at T0-T10, immediately giving a clue for a nonlinear rate of ROS formation during adipogenesis. This notion is more clearly established by the histograms depicted in Figure 4B, indicating an initial sudden increase in ROS formation at T3, followed by a marked decrease at T6 and a further increase at T10.

We next investigated the mechanism(s) of ROS formation associated with the different phases of the differentiation process and, for the reasons indicated in Section 1, tested the possibility of an involvement of NOX-2. This NOX enzyme, while predominant in macrophages, is also expressed in the adipose tissue<sup>52</sup> and animal studies document its importance in adipogenesis.<sup>16</sup> As indicated in Figure 4C, immunocytochemical evidence of NOX-2 activation was detected at the same time points in which an increased DCF fluorescence response was also observed (Figure 4B).

In order to investigate whether NOX-2 activation was paralleled by a mitochondrial mechanism of ROS formation, we also performed experiments using MitoSOX Red. Interestingly, the resulting fluorescence responses, while absent or negligible at T0-T6, increased significantly at T10 (Figure 4D,E). An indication of mitochondrial  $O_2^{\cdot-}$  formation is therefore obtained under conditions of maximal mitochondrial membrane hyperpolarization (Figure 3A) and cardiolipin oxidation (Figure 3B).

### 3.5 | Consequences of ROS formation during SW872 cell differentiation

We investigated Nrf2 expression in differentiating SW872 cells (Figure 5A) and observed a response characterized by a bimodal trend, reminiscent of that obtained in



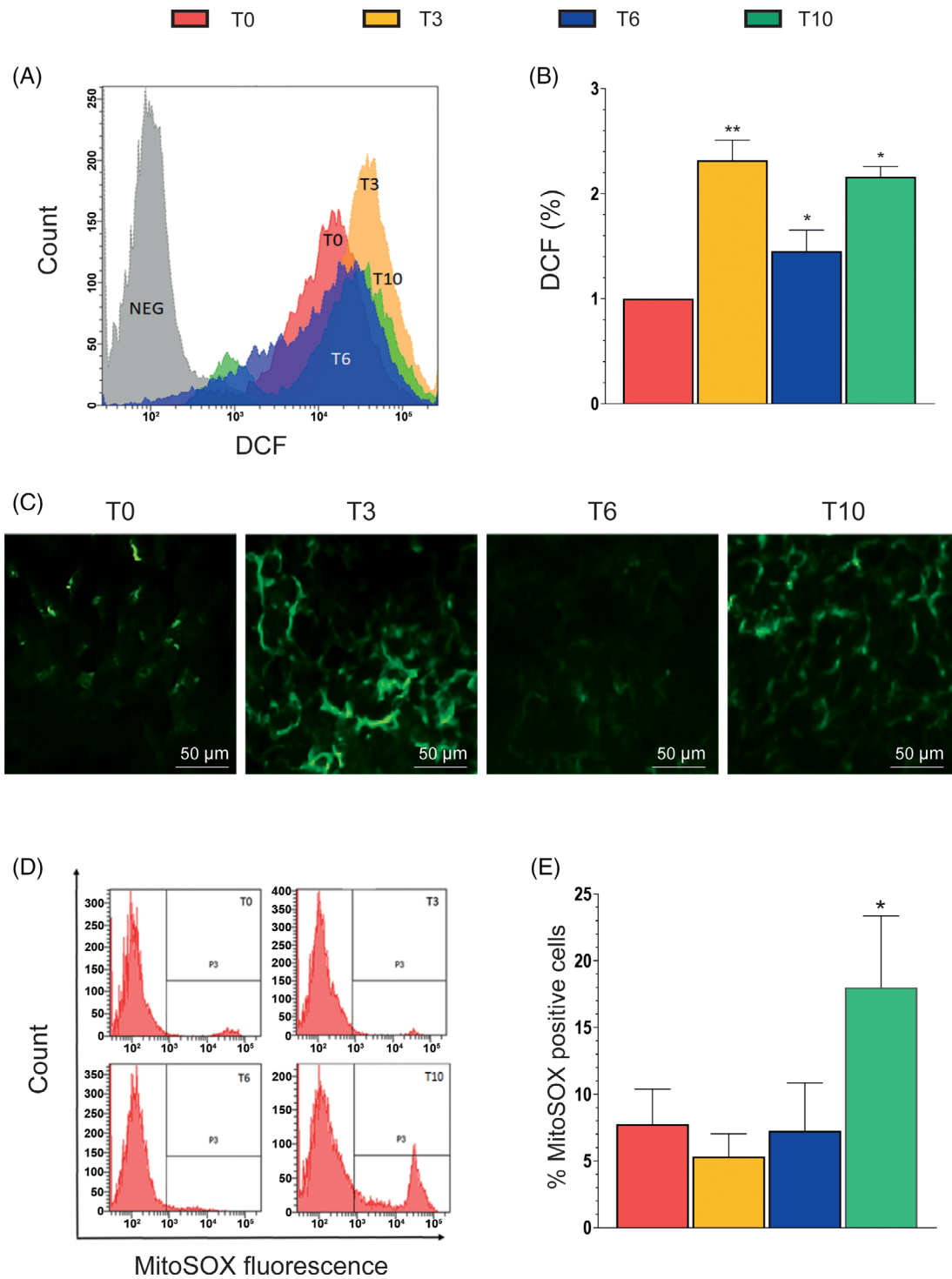


**FIGURE 4** Reactive oxygen species (ROS) production during differentiation. (A) Representative flow cytometry histograms of cells treated with the ROS-sensitive probe chloromethyl-2',7'-dichlorodihydrofluorescein diacetate (DCF). (B) Statistical analysis of the results obtained from different DCF flow cytometry assays. (C) Representative micrographs showing phosphorylated p47<sup>phox</sup> localization in SW872 cells. At the indicated times, the cells were fixed and analyzed for immunocytochemical detection of phosphorylated p47<sup>phox</sup>. (D) Representative flow cytometry histograms of cells treated with the mitochondrial ROS-sensitive probe MitoSOX Red. (E) Statistical analysis of the results from different MitoSOX Red flow cytometry analyses. Results represent the means  $\pm$  SD calculated from at least three independent determinations. \* $p < 0.05$ , \*\* $p < 0.01$ , as compared to the previous time point (one-way analysis of variance followed by Dunnett's test)

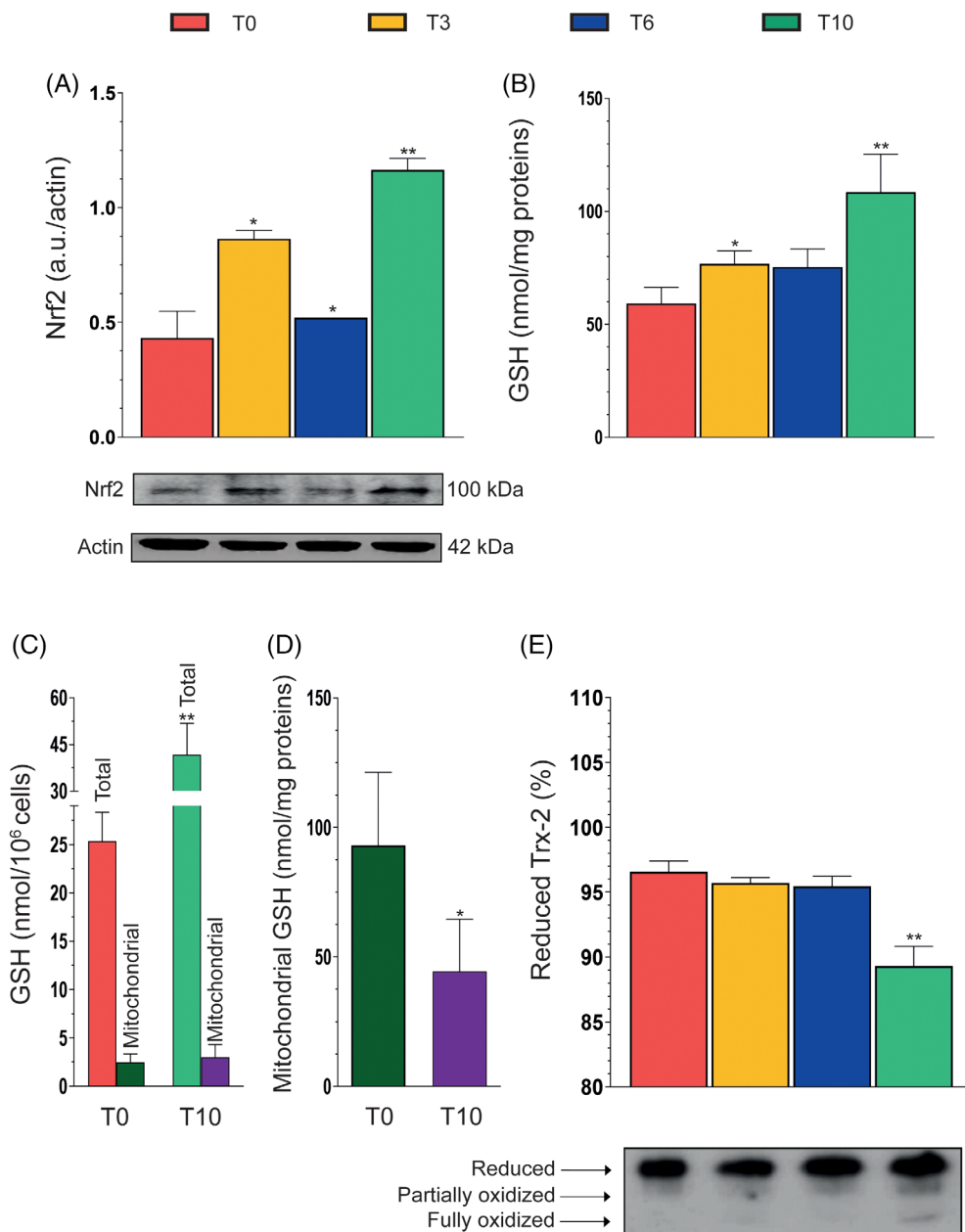


**FIGURE 5** Nuclear factor (erythroid-derived 2)-like 2 (Nrf2) expression, cellular/mitochondrial glutathione content, and thioredoxin 2 redox state during differentiation. (A) Western immunoblotting analysis of Nrf2 expression in differentiating SW872 cells. Actin was used as loading control. (B) Total glutathione (GSH) content at the indicated differentiation times. (C) Total and mitochondrial GSH content at T0 and T10. (D) GSH content of mitochondria isolated from cells at T0 and T10. (E) Analysis of reduced, partially oxidized, and fully oxidized thioredoxin 2 (Trx2) thiol groups at the indicated differentiation times. The redox state of Trx2 was determined by urea polyacrylamide gel electrophoresis under nonreducing conditions. Results represent the means  $\pm$  SD calculated from at least three independent determinations. \* $p < 0.05$ , \*\* $p < 0.01$ , as compared to the previous time point (one-way analysis of variance followed by Dunnett's test)

experiments measuring DCF fluorescence (Figure 4B). Consistently, an increase in total GSH was also observed at T3–T10 (Figure 5B), as  $\gamma$ -glutamine cysteine ligase, the rate-limiting enzyme of GSH biosynthesis, is over-expressed after Nrf2 activation.<sup>53</sup>

Based on the results shown in Figures 3B and 4E, respectively, providing evidence for a decline in cardiolipin expression and mitochondrial  $O_2^{\cdot-}$  formation at T10, we compared the levels of total GSH and mitochondrial GSH (mGSH) at T0 versus T10.

It was interesting to observe that, when normalized on cell number, the increase in total GSH detected at T10 is not paralleled by a similar increase in mGSH, which actually remained virtually unchanged with respect to that detected at T0 (Figure 5C). Consistently, when the data

were expressed as nmol/mg proteins, mGSH was significantly lower at T10 versus T0 (Figure 5C). These results are therefore indicative of an extensive mitochondrial  $O_2^{\cdot-}$  formation, a notion also consistent with the outcome of studies investigating the level of Trx2 oxidation, an important mitochondrial redox regulator.<sup>42</sup> We performed a redox gel using anti-Trx 2 antibodies and obtained evidence of significant Trx2 oxidation at T10, with hardly any effect being observed at T3 or T6 (Figure 5D).

## 4 | DISCUSSION

Adipocyte differentiation is a complex process characterized by a highly ordered and well-defined temporal

sequence. In this study, we performed a detailed characterization of the morphological changes associated with the differentiation of postconfluent human SW872 cells grown in a conventional DM. We obtained evidence for a time-dependent conversion of a very large proportion of the preadipocytes to fully differentiated adipocytes. This process, apparently completed at T6, was paralleled by the progressive accumulation of cells in the G0/G1 phase, and expression of specific transcription factors and differentiation markers was involved in the induction phase, as C/EBP $\beta$  and C/EBP $\delta$ , or the late phase, as PPAR $\gamma$  and CD36.

More specifically, we obtained evidence for a constitutive expression, further increased at T3 and T6, of C/EBP $\beta$ , which is associated with an intracellular redistribution of the protein, initially exclusively localized in nuclei. These results are in keeping with the findings from other studies.<sup>54,55</sup>

The kinetics of C/EBP $\delta$  expression was instead somewhat unexpected and different from those obtained in other studies using different models of adipogenesis.<sup>54</sup> Indeed, C/EBP $\delta$  was scarcely detectable at the early stages of differentiation (T0 and T3), and its expression increased significantly in the late stages of differentiation (T6 and T10), in parallel with a subcellular redistribution of the protein.

C/EBP $\beta$ , unlike C/EBP $\delta$  protein expression, seemed to precede the expression of PPAR $\gamma$ , which increased significantly at T3, with maintenance of similar levels at T6 and T10. CD36, a multifunctional protein and a target gene of PPAR $\gamma$ , presented an expression pattern similar to that of PPAR $\gamma$ .<sup>56</sup>

In short, SW872 cells well differentiate to mature adipocytes when grown in DM and the morphological changes observed during this process were accompanied by the expression of early and late markers of differentiation, which followed kinetics similar to the ones reported in other cellular model of adipocyte differentiation,<sup>54,55</sup> however with the exception of C/EBP $\delta$ .

The process of adipocyte differentiation is associated with an increased mitochondrial biogenesis, which is needed to support various key functions of the mature adipocytes.<sup>57</sup> Increased mitochondriogenesis is often associated with an increase in mitochondrial membrane potential.<sup>58,59</sup> Consistently, a progressive increase in mitochondrial mass/number was observed during the course of SW872 cell adipogenesis. We also observed a rather dramatic increase in mitochondrial membrane potential, indicative of an active mitochondrial formation of ROS.<sup>60</sup> Our data on cardiolipin expression, showing a progressive increase followed by a sudden drop at day 10, are therefore consistent with both the data on mitochondrial mass/number and with the robust increase in mitochondrial O<sub>2</sub><sup>-</sup> formation detected at T10.

The involvement of ROS in the adipogenic process is documented by numerous studies using different cellular models.<sup>61–63</sup> In this study, we obtained evidence for an intermittent formation of ROS during SW872 cell adipogenesis, likely attributable to NOX-2 activation, requiring interaction of the membrane and cytosolic subunits to generate O<sub>2</sub><sup>-</sup>, rapidly converted to diffusible H<sub>2</sub>O<sub>2</sub>.<sup>64</sup> Indeed, our immunofluorescence studies using anti-p47<sup>phox</sup> antibodies were indicative of a significant NOX-2 activation at T3, virtual loss of activity at T6, and again activation at T10, that is, an intermittent activation pattern superimposable on the kinetic of ROS formation measured with DCF.

These results are therefore consistent with the possibility that early NOX-2 activation plays a role in SW872 cell adipogenic differentiation, a conclusion in keeping with the outcome of *in vivo* studies using NOX-2-deficient mice.<sup>22,23</sup>

In this study, we did not investigate NOX-4 expression and activity during differentiation, which in any case appears likely since this NOX enzyme displays enhanced expression in response to H<sub>2</sub>O<sub>2</sub>.<sup>15</sup> This suggests the possibility of a crosstalk between NOX-2 and NOX-4. However, a crosstalk is also likely to take place between the NOX enzymes and mROS.<sup>15</sup> We observed a late onset mitochondrial O<sub>2</sub><sup>-</sup> formation, thereby implying that at least two different mechanisms contribute to the DCF-fluorescence response detected at T10, one based on NOX-2 activation and another one associated with mitochondrial events. These results are consistent with the possibility that late NOX-2 activity participates in the triggering of late mitochondrial O<sub>2</sub><sup>-</sup> emission.

It is important to note that the apparent absence of mROS formation at T3 and T6 is rather surprising since other reports provided evidence for the formation of these species during the early phases of adipogenesis.<sup>65</sup> In addition, as indicated earlier, an excessive supply of energy substrates to metabolic pathways should induce the production of ROS and, more specifically, oversupply of electrons to the respiratory chain should increase mitochondrial O<sub>2</sub><sup>-</sup> formation.<sup>14,15</sup>

One good reason that might explain the absence of detectable mROS at T3 and T6 is, however, based on the increased expression of Nrf2, readily activated after ROS-dependent oxidation of the Nrf2 inhibitor Kelch-like ECH-associated protein 1.<sup>66</sup> Upregulated Nrf2 promotes the expression of multiple antioxidant genes involved in different functions, which include mitochondrial H<sub>2</sub>O<sub>2</sub> detoxification.<sup>67</sup> One of these genes encodes for  $\gamma$ -glutamine cysteine ligase, the rate-limiting enzyme of GSH biosynthesis.<sup>53</sup> This event takes place in the cytosol and is followed by a subcellular distribution of the tripeptide in different compartments, for example, nuclei,

endoplasmic reticulum, and mitochondria.<sup>68</sup> Interestingly, the cytosolic and mitochondrial concentrations of GSH are remarkably similar (1–10 mM).<sup>69</sup> Cytosol-to-mGSH translocation takes place via poorly defined mitochondrial carriers,<sup>70,71</sup> in some studies identified in the dicarboxylate and 2-oxoglutarate carriers (rat liver and kidney),<sup>71,72</sup> or tricarboxylate carrier (rat brain).<sup>73</sup> mGSH represents a key player of the mitochondrial antioxidant defense, actively regulating the redox status of these organelles via different mechanisms, in particular by acting as a cofactor for glutathione peroxidase.<sup>74</sup> An additional important mitochondrial antioxidant defense is represented by the Trx 2/Trx reductase 2 system.<sup>75</sup>

In our experiments, Nrf2 activation was detected under the same conditions in which ROS were generated by early NOX-2-activation, and late events in which NOX-2 and mitochondria were concomitantly involved. Consistently, an increase in total GSH was also detected at T3 and T10. Based on these findings, the early Nrf2 response, while possibly stimulated by NOX-2-derived ROS, should provide a general protection to the differentiating adipocytes and may account for an efficient scavenging of mROS at T3 and T6.

The scenario drastically changed at T10, a time at which mROS formation was possibly associated with mitochondrial dysfunction. At T3 and T6, we observed parallel increases in cardiolipin levels and mitochondrial mass/number, but at T10 cardiolipin levels decreased despite the further increase in mitochondrial mass/number. This is indicative of cardiolipin oxidation, since this protein is highly susceptible to oxidative damage.<sup>76</sup> At T10, we also obtained evidence for a decline in mGSH levels, despite the significant rise in the overall cellular concentration of the tripeptide. This is also indicative of extensive mROS formation, apparently causing a decrease in mGSH, which cannot be compensated by the increased GSH biosynthesis driven by the Nrf2 response. The synthesis of GSH indeed takes place in the cytosol, and its transport in mitochondria limits the accumulation of the tripeptide in these organelles.<sup>77</sup>

The third observation providing indirect evidence of mROS formation at T10 is based on the extensive Trx2 oxidation detected at this time point. In addition, in keeping with the results of experiments using MitoSOX Red fluorescence to detect O<sub>2</sub><sup>•-</sup> formation, there was no evidence of Trx2 oxidation at T3 or T6.

In conclusion, the results presented in this study provide a detailed characterization of the biochemical and morphological changes of differentiating SW872 cells as well as an indication for an intermittent release of ROS mediated by different mechanisms. Our results are indicative of a complex regulation of ROS formation during differentiation of these cells, with the NOX enzymes

likely involved in the regulation of the adipogenic process. We provide evidence for an early increase in NOX-2 activity, which might imply a role of NOX-2-derived O<sub>2</sub><sup>•-</sup> in adipogenesis, although a critical link between this event and delayed mROS formation is also likely to occur. This second mechanism of ROS formation, probably as a consequence of the Nrf2-dependent adaptive response, was uniquely detected at T10, and, at least in the conditions employed in this study, does not appear to play a major role in the induction of adipogenesis, apparently completed at T6. mROS are instead likely involved with the induction of mitochondrial dysfunction.

## ACKNOWLEDGMENT

This study was supported by Ricerca Finalizzata—Ministero della salute 2018 (RF-2016-02363761)—Italy.

## CONFLICT OF INTEREST

The authors declare no potential conflict of interest.

## DATA AVAILABILITY STATEMENT

The data that support the findings of this study are available from the corresponding author upon reasonable request.

## ORCID

Mara Fiorani  <https://orcid.org/0000-0003-0310-2670>

Orazio Cantoni  <https://orcid.org/0000-0002-7182-802X>

## REFERENCES

- Kojta I, Chacinska M, Blachnio-Zabielska A. Obesity, bioactive lipids, and adipose tissue inflammation in insulin resistance. *Nutrients*. 2020;12:1305.
- Fuster JJ, Ouchi N, Gokce N, Walsh K. Obesity-induced changes in adipose tissue microenvironment and their impact on cardiovascular disease. *Circ Res*. 2016;118:1786–1807.
- Corona-Meraz FI, Robles-De Anda JA, Madrigal-Ruiz P-M, Díaz-Rubio G-I, Castro-Albarrán J, Navarro-Hernández R-E. In: Çakmur H, editor. *Obesity*. London: Intechopen; 2020.
- Manna P, Jain SK. Obesity, oxidative stress, adipose tissue dysfunction, and the associated health risks: causes and therapeutic strategies. *Metab Syndr Relat Disord*. 2015;13:423–444.
- McMurray F, Patten DA, Harper ME. Reactive oxygen species and oxidative stress in obesity-recent findings and empirical approaches. *Obesity (Silver Spring)*. 2016;24:2301–2310.
- Haslam DW, James WP. *Obesity*. *Lancet*. 2005;366:1197–1209.
- Grundy SM, Brewer HB Jr, Cleeman JI, Smith SC Jr, Lenfant C, American Heart Association, et al. Definition of metabolic syndrome: report of the National Heart, Lung, and Blood Institute/American Heart Association conference on scientific issues related to definition. *Circulation*. 2004;109:433–438.
- Rangwala SM, Lazar MA. Transcriptional control of adipogenesis. *Annu Rev Nutr*. 2000;20:535–559.
- Lefterova MI, Lazar MA. New developments in adipogenesis. *Trends Endocrinol Metab*. 2009;20:107–114.



10. Calzadilla P, Sapochnik D, Cosentino S, Diz V, Dixelio L, Calvo JC, et al. N-acetylcysteine reduces markers of differentiation in 3T3-L1 adipocytes. *Int J Mol Sci.* 2011;12:6936–6951.
11. Totan BR, Baygut H, Karada MG. Vitamin C physiology: the known and the unknown in obesity. *J Food Nutr Res.* 2019;7: 613–618.
12. de Villiers D, Potgieter M, Ambele MA, Adam L, Durandt C, Pepper MS. The role of reactive oxygen species in adipogenic differentiation. *Adv Exp Med Biol.* 2018;1083:125–144.
13. Castro JP, Grune T, Speckmann B. The two faces of reactive oxygen species (ROS) in adipocyte function and dysfunction. *Biol Chem.* 2016;397:709–724.
14. Wellen KE, Thompson CB. Cellular metabolic stress: considering how cells respond to nutrient excess. *Mol Cell.* 2010;40: 323–332.
15. Jankovic A, Korac A, Buzadzic B, Otasevic V, Stancic A, Daiber A, et al. Redox implications in adipose tissue (dys)function—a new look at old acquaintances. *Redox Biol.* 2015;6: 19–32.
16. DeVallance E, Li Y, Jurczak MJ, Cifuentes-Pagano E, Pagano PJ. The role of NADPH oxidases in the etiology of obesity and metabolic syndrome: contribution of individual isoforms and cell biology. *Antioxid Redox Signal.* 2019;31: 687–709.
17. Han CY. Roles of reactive oxygen species on insulin resistance in adipose tissue. *Diabetes Metab J.* 2016;40:272–279.
18. Schroder K, Wandzioch K, Helmcke I, Brandes RP. Nox4 acts as a switch between differentiation and proliferation in pre-adipocytes. *Arterioscler Thromb Vasc Biol.* 2009;29:239–245.
19. Liu GS, Chan EC, Higuchi M, Dusing GJ, Jiang F. Redox mechanisms in regulation of adipocyte differentiation: beyond a general stress response. *Cell.* 2012;1:976–993.
20. Catalán V, Gómez-Ambrosi J, Rodríguez A, Ramírez B, Rotellar F, Valentí V, et al. Increased levels of calprotectin in obesity are related to macrophage content: impact on inflammation and effect of weight loss. *Mol Med.* 2011;17:1157–1167.
21. Sakurai T, Izawa T, Kizaki T, Ogasawara JE, Shirato K, Imaizumi K, et al. Exercise training decreases expression of inflammation-related adipokines through reduction of oxidative stress in rat white adipose tissue. *Biochem Biophys Res Commun.* 2009;379:605–609.
22. Pepping JK, Freeman LR, Gupta S, Keller JN, Bruce-Keller AJ. NOX2 deficiency attenuates markers of adiposopathy and brain injury induced by high-fat diet. *Am J Physiol Endocrinol Metab.* 2013;304:E392–404.
23. Ronis MJ, Sharma N, Vantrease J, Borengasser SJ, Ferguson M, Mercer KE, et al. Female mice lacking p47phox have altered adipose tissue gene expression and are protected against high fat-induced obesity. *Physiol Genomics.* 2013;45:351–366.
24. Li Y, Mouche S, Sajic T, Veyrat-Durebex C, Supale R, Pierroz D, et al. Deficiency in the NADPH oxidase 4 predisposes towards diet-induced obesity. *Int J Obes (Lond).* 2012;36:1503–1513.
25. Ruiz-Ojeda FJ, Ruperez AI, Gomez-Llorente C, Gil A, Aguilera CM. Cell models and their application for studying adipogenic differentiation in relation to obesity: a review. *Int J Mol Sci.* 2016;17:1040.
26. Tung YC, Hsieh PH, Pan MH, Ho CT. Cellular models for the evaluation of the antiobesity effect of selected phytochemicals from food and herbs. *J Food Drug Anal.* 2017;25:100–110.
27. Burton GR, Nagarajan R, Peterson CA, McGehee RE Jr. Microarray analysis of differentiation-specific gene expression during 3T3-L1 adipogenesis. *Gene.* 2004;329:167–185.
28. Madsen L, Petersen RK, Sørensen MB, Jørgensen C, Hallenborg P, Priddel L, et al. Adipocyte differentiation of 3T3-L1 preadipocytes is dependent on lipoxygenase activity during the initial stages of the differentiation process. *Biochem J.* 2003;375:539–549.
29. Samuni Y, Cook JA, Choudhuri R, DeGraff W, Sowers AL, Krishna MC, et al. Inhibition of adipogenesis by Tempol in 3T3-L1 cells. *Free Radic Biol Med.* 2010;49:667–673.
30. Qian SW, Li X, Zhang YY, Huang HY, Liu Y, Sun X, et al. Characterization of adipocyte differentiation from human mesenchymal stem cells in bone marrow. *BMC Dev Biol.* 2010; 10:47.
31. Yin C, Xiao Y, Zhang W, Xu E, Liu W, Yi X, et al. DNA microarray analysis of genes differentially expressed in adipocyte differentiation. *J Biosci.* 2014;39:415–423.
32. Lefterova MI, Haakonsson AK, Lazar MA, Mandrup S. PPARGgamma and the global map of adipogenesis and beyond. *Trends Endocrinol Metab.* 2014;25:293–302.
33. Zhao XY, Chen XY, Zhang ZJ, Kang Y, Liao WM, Yu WH, et al. Expression patterns of transcription factor PPARGgamma and C/EBP family members during in vitro adipogenesis of human bone marrow mesenchymal stem cells. *Cell Biol Int.* 2015;39:457–465.
34. Vassiliou G, Benoist F, Lau P, Kavaslar GN, McPherson R. The low density lipoprotein receptor-related protein contributes to selective uptake of high density lipoprotein cholesteryl esters by SW872 liposarcoma cells and primary human adipocytes. *J Biol Chem.* 2001;276:48823–48830.
35. Stratford EW, Castro R, Daffinrud J, Skarn M, Lauvrak S, Munthe E, et al. Characterization of liposarcoma cell lines for preclinical and biological studies. *Sarcoma.* 2012;2012:148614.
36. Nativel B, Marimoutou M, Thon-Hon VG, Gunasekaran MK, Andries J, Stanislas G, et al. Soluble HMGB1 is a novel adipokine stimulating IL-6 secretion through RAGE receptor in SW872 preadipocyte cell line: contribution to chronic inflammation in fat tissue. *PLoS One.* 2013;8:e76039.
37. Gauthier A, Vassiliou G, Benoist F, McPherson R. Adipocyte low density lipoprotein receptor-related protein gene expression and function is regulated by peroxisome proliferator-activated receptor gamma. *J Biol Chem.* 2003;278:11945–11953.
38. Greene DJ, Izem L, Morton RE. Defective triglyceride biosynthesis in CETP-deficient SW872 cells. *J Lipid Res.* 2015;56: 1669–1678.
39. Koopman R, Schaart G, Hesselink MK. Optimisation of oil red O staining permits combination with immunofluorescence and automated quantification of lipids. *Histochem Cell Biol.* 2001; 116:63–68.
40. Fiorani M, Guidarelli A, Capellacci V, Cerioni L, Crinelli R, Cantoni O. The dual role of mitochondrial superoxide in arsenite toxicity: signaling at the boundary between apoptotic commitment and cytoprotection. *Toxicol Appl Pharmacol.* 2018; 345:26–35.
41. Guidarelli A, Cerioni L, Fiorani M, Catalani A, Cantoni O. Arsenite-induced mitochondrial superoxide formation: time and concentration requirements for the effects of the metalloid on the endoplasmic reticulum and mitochondria. *J Pharmacol Exp Ther.* 2020;373:62–71.

42. Folda A, Citta A, Scalcon V, Cali T, Zonta F, Scutari G, et al. Mitochondrial thioredoxin system as a modulator of cyclophilin D redox state. *Sci Rep.* 2016;6:23071.
43. Fiorani M, Scotti M, Guidarelli A, Burattini S, Falcieri E, Cantoni O. SVCT2-dependent plasma and mitochondrial membrane transport of ascorbic acid in differentiating myoblasts. *Pharmacol Res.* 2020;159:105042.
44. Brundu S, Nencioni L, Celestino I, Coluccio P, Palamara AT, Magnani M, et al. Validation of a reversed-phase high performance liquid chromatography method for the simultaneous analysis of cysteine and reduced glutathione in mouse organs. *Oxid Med Cell Longev.* 2016;2016:1746985.
45. Kauffman ME, Kauffman MK, Traore K, Zhu H, Trush MA, Jia Z, et al. MitoSOX-based flow cytometry for detecting mitochondrial ROS. *React Oxyg Species.* 2016;2:361–370.
46. Wojtala A, Bonora M, Malinska D, Pinton P, Duszynski J, Wieckowski MR. Methods to monitor ROS production by fluorescence microscopy and fluorometry. *Methods Enzymol.* 2014;542:243–262.
47. Canonico B, Cesarini E, Salucci S, Luchetti F, Falcieri E, di Sario G, et al. Defective autophagy, mitochondrial clearance and lipophagy in Niemann-pick type B lymphocytes. *PLoS One.* 2016;11:e0165780.
48. Benedetti S, Catalani S, Palma F, Canonico B, Luchetti F, Galati R, et al. Acyclovir induces cell cycle perturbation and apoptosis in Jurkat leukemia cells, and enhances chemotherapeutic drug cytotoxicity. *Life Sci.* 2018;215:80–85.
49. Mehlem A, Hagberg CE, Muhl L, Eriksson U, Falkevall A. Imaging of neutral lipids by oil red O for analyzing the metabolic status in health and disease. *Nat Protoc.* 2013;8:1149–1154.
50. Hagberg CE, Li Q, Kutschke M, Bhowmick D, Kiss E, Shabalina IG, et al. Flow cytometry of mouse and human adipocytes for the analysis of browning and cellular heterogeneity. *Cell Rep.* 2018;24:e2745.
51. Asumendi A, Morales MC, Alvarez A, Arechaga J, Perez-Yarza G. Implication of mitochondria-derived ROS and cardioplipin peroxidation in N-(4-hydroxyphenyl)retinamide-induced apoptosis. *Br J Cancer.* 2002;86:1951–1956.
52. Leloup C, Casteilla L, Carrière A, Galinier A, Benani A, Carneiro L, et al. Balancing mitochondrial redox signaling: a key point in metabolic regulation. *Antioxid Redox Signal.* 2011;14:519–530.
53. Wild AC, Moinova HR, Mulcahy RT. Regulation of gamma-glutamylcysteine synthetase subunit gene expression by the transcription factor Nrf2. *J Biol Chem.* 1999;274:33627–33636.
54. Wu Z, Xie Y, Morrison RF, Bucher NL, Farmer SR. PPARgamma induces the insulin-dependent glucose transporter GLUT4 in the absence of C/EBPalpha during the conversion of 3T3 fibroblasts into adipocytes. *J Clin Invest.* 1998;101:22–32.
55. Farmer SR. Transcriptional control of adipocyte formation. *Cell Metab.* 2006;4:263–273.
56. Gao H, Li D, Yang P, Zhao L, Wei L, Chen Y, et al. Suppression of CD36 attenuates adipogenesis with a reduction of P2X7 expression in 3T3-L1 cells. *Biochem Biophys Res Commun.* 2017;491:204–208.
57. Wilson-Fritch L, Burkart A, Bell G, Mendelson K, Leszyk J, Nicoloso S, et al. Mitochondrial biogenesis and remodeling during adipogenesis and in response to the insulin sensitizer rosiglitazone. *Mol Cell Biol.* 2003;23:1085–1094.
58. Hofmann AD, Beyer M, Krause-Buchholz U, Wobus M, Bornhäuser M, Rödel G. OXPHOS supercomplexes as a hallmark of the mitochondrial phenotype of adipogenic differentiated human MSCs. *PLoS One.* 2012;7:e35160.
59. Zhang Y, Marsboom G, Toth PT, Rehman J. Mitochondrial respiration regulates adipogenic differentiation of human mesenchymal stem cells. *PLoS One.* 2013;8:e77077.
60. Suski J, Lebieczinska M, Bonora M, Pinton P, Duszynski J, Wieckowski MR. Relation between mitochondrial membrane potential and ROS formation. *Methods Mol Biol.* 2018;1782:57–381.
61. Atashi F, Modarressi A, Pepper MS. The role of reactive oxygen species in mesenchymal stem cell adipogenic and osteogenic differentiation: a review. *Stem Cells Dev.* 2015;24:1150–1163.
62. Wang W, Zhang Y, Lu W, Liu K. Mitochondrial reactive oxygen species regulate adipocyte differentiation of mesenchymal stem cells in hematopoietic stress induced by arabinosylcytosine. *PLoS One.* 2015;10:e0120629.
63. Lee H, Lee YJ, Choi H, Ko EH, Kim JW. Reactive oxygen species facilitate adipocyte differentiation by accelerating mitotic clonal expansion. *J Biol Chem.* 2009;284:10601–10609.
64. Panday A, Sahoo MK, Osorio D, Batra S. NADPH oxidases: an overview from structure to innate immunity-associated pathologies. *Cell Mol Immunol.* 2015;12:5–23.
65. Tormos KV, Anso E, Hamanaka RB, Eisenbart J, Joseph J, Kalyanaraman B, et al. Mitochondrial complex III ROS regulate adipocyte differentiation. *Cell Metab.* 2011;14:537–544.
66. Kovac S, Angelova PR, Holmström KM, Zhang Y, Dinkova-Kostova AT, Abramov AY. Nrf2 regulates ROS production by mitochondria and NADPH oxidase. *Biochim Biophys Acta.* 2015;1850:794–801.
67. Dinkova-Kostova AT, Abramov AY. The emerging role of Nrf2 in mitochondrial function. *Free Radic Biol Med.* 2015;88:179–188.
68. Circu ML, Aw TY. Glutathione and modulation of cell apoptosis. *Biochim Biophys Acta.* 2012;1823:1767–1777.
69. Meister A, Anderson ME. Glutathione. *Annu Rev Biochem.* 1983;52:711–760.
70. Booty LM, King MS, Thangaratnarajah C, Majd H, James AM, Kunji ERS, et al. The mitochondrial dicarboxylate and 2-oxoglutarate carriers do not transport glutathione. *FEBS Lett.* 2015;589:621–628.
71. Bachhawat AK, Thakur A, Kaur J, Zulkifli M. Glutathione transporters. *Biochim Biophys Acta.* 2013;1830:3154–3164.
72. Mari M, Morales A, Colell A, Garcia-Ruiz C, Fernandez-Checa JC. Mitochondrial glutathione, a key survival antioxidant. *Antioxid Redox Signal.* 2009;11:2685–2700.
73. Kamga CK, Zhang SX, Wang Y. Dicarboxylate carrier-mediated glutathione transport is essential for reactive oxygen species homeostasis and normal respiration in rat brain mitochondria. *Am J Physiol Cell Physiol.* 2010;299:C497–505.
74. Handy DE, Loscalzo J. Redox regulation of mitochondrial function. *Antioxid Redox Signal.* 2012;16:1323–1367.
75. Jaganjac M, Milkovic L, Sunjic SB, Zarkovic N. The NRF2, thioredoxin, and glutathione system in tumorigenesis and anticancer therapies. *Antioxidants.* 2020;9:1151.
76. Paradies G, Paradies V, Ruggiero FM, Petrosillo G. Oxidative stress, cardioplipin and mitochondrial dysfunction in



nonalcoholic fatty liver disease. *World J Gastroenterol.* 2014; 20:14205–14218.

77. Calabrese G, Morgan B, Riemer J. Mitochondrial glutathione: regulation and functions. *Antioxid Redox Signal.* 2017;27:1162–1177.

### SUPPORTING INFORMATION

Additional supporting information may be found online in the Supporting Information section at the end of this article.

**How to cite this article:** Fiorani M, De Matteis R, Canonico B, Blandino G, Mazzoli A, Montanari M, et al. Temporal correlation of morphological and biochemical changes with the recruitment of different mechanisms of reactive oxygen species formation during human SW872 cell adipogenic differentiation. *BioFactors.* 2021;47:837–51. <https://doi.org/10.1002/biof.1769>